Microstructure Investigation and Mechanical Properties of Coated Zircaloy Cladding

Nuclear Technology Research and Development

Prepared for
U.S. Department of Energy
Tim Graening
Caleb P. Massey
Kory Linton
Andrew Nelson
Oak Ridge National Laboratory

06/30/2021
M2FT-21OR020202011
ORNL/SPR-2021/2038

SUMMARY

Accident Tolerant Fuel concepts have been developed and tested in diverse research programs presently around the world. Industry teams have developed proprietary coating compositions and geometries, but significant knowledge gaps exist in terms of the resulting properties of the coating and the cladding and how those components impact each other in reactor conditions. Furthermore, the national laboratory and university teams currently studying the industry concepts are limited in their ability to freely disseminate and discuss results obtained on commercial coatings. The Advanced Fuels Campaign is therefore working to develop an understanding of 'generic' coatings applied to commercial nuclear cladding alloys free of these constraints. This milestone report provides insights in the microstructure of a 7-micrometer Cr coating on Zircaloy-2 and a 5-micrometer coating on Zry-4 as reference materials. SEM and TEM methods were utilized to describe and identify the interface, while nanoindentation was used to determine hardness and E-Moduli of coating and cladding material. This milestone summarizes the acquired knowledge to build a necessary verified foundation for future simulation and qualification efforts.

CONTENTS

FIGURES

TABLES

ACRONYMS

ASTM	American Society for Testing and Materials
ATF	accident-tolerant fuel
BCC	base centered cubic
BISON	a finite element–based nuclear fuel performance code
BWR	boiling water reactor
CTE	coefficient of thermal expansion
CVD	chemical vapor deposition
EBSD	electron backscatter diffraction
EDS	energy-dispersive x-ray spectroscopy
EFTEM	energy-filtered transmission electron microscopy
FEM	finite element method
HAADF	High Angle Annular Dark Field
HFIR	High Flux Isotope Reactor
HiPIMS	high-power impulse magnetron sputtering
IFEL	Irradiated Fuels Examination Facility
LFA	laser flash analysis
LOCA	loss-of-coolant accident
LWR	light-water reactor
MBT	modified burst test
ORNL	Oak Ridge National Laboratory
PVD	physical vapor deposition
PWR	pressurized water reactor
SATS	Severe Accident Test Station
SEM	scanning electron microscopy
STEM	scanning transmission electron microscopy
TEM	transmission electron microscopy
UTS	ultimate tensile strength
XRD	x-ray diffraction
YS	yield strength
ZIRLO	advanced zirconium-based alloy by Westinghouse
Zry-2	Zircaloy-2
Zry-4	Zircaloy-4

MICROSTRUCTURE AND MECHANICAL PROPERTIES OF COATED ZIRCALOY CLADDING

1. INTRODUCTION

Research on accident tolerant fuels (ATF) has started after the Fukoshima accident [1–3]. While efforts have been expended on both fuel and cladding ATF concepts, the bulk of work has been devoted to improved cladding. The overarching goal of these approaches is to enhance the high-temperature behavior of the cladding. Complete replacement of Zr alloys through either iron-chromium-aluminum (FeCrAl) or silicon carbide composite (SiC/SiC) represent more aggressive approaches to this challenge. The most basic ATF cladding concept is obtained by applying a thin coating of highly corrosion-resistant material on the cladding's surface. This thin coating is intended to not interfere with the neutronic or mechanical performance of the base cladding under normal operating conditions. Different coating materials, thicknesses, coating processes, process parameters, and testing methods have an impact on the microstructure and mechanical properties and therefore on the results of the applied investigation methods, which makes the licensing of a selected coating cumbersome [4]. A large variety of methods have been developed to investigate coatings for cladding materials and their mechanical properties [5–9]. Coated zirconium cladding concepts have grown to become prioritized approaches of industry ATF efforts. Licensure of coated zirconium cladding would presumably be less costly and time-consuming than FeCrAl or SiC/SiC; this is logically consistent as failure of the coating would then result in the same base cladding concept that is already licensed (assuming that no credit is taken for coating performance). The challenge for the research and regulatory community is that vendor coating concepts are all proprietary, and highly bound by restrictions on data distribution. Many Advanced Fuels Campaign (AFC) national laboratories are actively collecting data for all U.S. fuel vendors' coated cladding concepts, but dissemination and discussion of these results in an open format is not possible. This limitation has prompted AFC to invest in independently sourced coatings free of these restrictions. Success in producing these coated Zr cladding materials will enable material investigations, basic property studies, failure modes, and other attributes for discussion in the open literature. The availability of this data will enhance technical discussion across vendor teams and dialogue with regulatory bodies. This report focuses on the microstructure characterization of FY21 Cr-coating with a thickness of around 6 to 7 μm as created by physical vapor deposition (PVD) on Zircaloy-2 claddings and 5-micrometer Cr coatings on Zry-4 tubes. Chromium coating have been chosen for this study due to their outstanding corrosion resistance under normal operating temperatures and a good oxidation resistance under accident conditions. While not all U.S. vendors use Cr metal coatings, it is more common than other Cr-containing coating materials and represents the best choice of an initial 'generic' coating material for initial optimization studies.

Figure 1 shows the coating morphology based on the substrate temperature, kinetic energy of ions, and the deposition rate [10], and it also demonstrates an understanding of how the coating morphology can be tailored so that it excels in crucial areas such as the residual stress state of the coating and thermal and irradiation creep. This report gives insights into the microstructure of (high-power impulse magnetron sputtering) HiPIMS PCD coated Cr on Zircaloy. Data on application-relevant testing of coated claddings in reactor-relevant environments will be gathered in future studies [9,11–13]. Ultimate exploration of the impact of Cr coatings on cladding performance will require irradiation. This report summarizes results acquired using SEM, TEM, and nanoindentation methods. However, initial work will focus on unirradiated performance testing. The results of the microstructure characterization can be used to investigate the eutectic penetration, thermal and irradiation creep, failure mechanisms, plastic deformation, elastic modulus, and oxidation behavior.

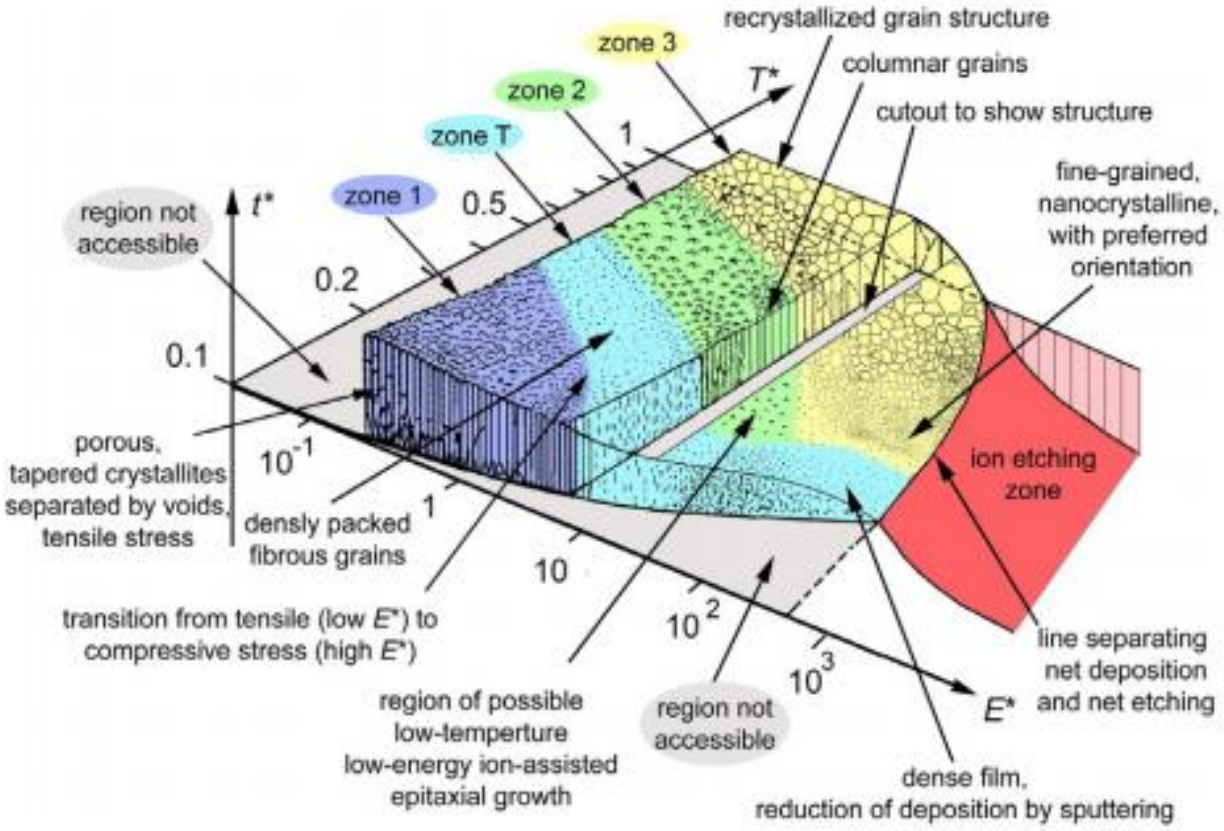

Figure 1. Generalized Structure Zone Diagram [10].

2. MATERIALS

Zircaloy-2 tubes have been used in boiling water reactors (BWR) for past decades. The investigated coated Zircaloy-2 and Zircaloy-4 tubes were cut into 12" segments. The nominal chemical composition is listed in Table 1.

Table 1. Dimension and nominal chemical composition of Zircaloy-2 and Zircaloy-4.

Parameter	Zircaloy-2[a]	Zircaloy-4[b]
Length, mm	30.48	30.48
Width, mm	10.00	9.50
Thickness, mm	0.65	0.56
Zr, wt.%	Balance	Balance
Sn, wt.%	1.20–1.70	1.20–1.45
Fe + Cr + Ni, wt.%	0.18–0.38	0.37 (no Ni)
Cr, wt.%	0.05–0.15	0.07–0.13
Ni, wt.%	0.03–0.08	-

[a]ASTM B350; [b]ASTM B353

The Cr-coating was applied using a HiPIMS process at Acree Technologies Inc. in California. Before the mounting of the 12" Zry-tubes in the PVD coating machine, the tubes were cleaned using an ultrasonic cleaner and isopropanol. After mounting, a plasma cleaning step was conducted to clean the surface of the cladding tubes. The applied bias voltage during the coating process was -35V and the temperature was about 150 °C. A growth rate of around 1nm per hour was achieved. The relatively low coating temperature was chosen to ensure that thermal expansion differences between the Cr coating and the Zircaloy cladding material is not negatively impacting the properties of the coating, while ensuring to create a microstructure similar to zone T shown in Figure 1.

3. COATING FABRICATION AND MICROSTRUCTURE INVESTIGATION

ORNL procured several hundred meters of Zry-4 from Cameco Fuel Manufacturing (Port Hope, Ontario, Canada) in FY20. The material was stress relieved and conformed to the typical geometry of a pressurized water reactor cladding, conforming to ASTM B353-12. Product certifications are on file at ORNL. Zry-2 was obtained from archive material at ORNL. The material was also stress relieved and conforms to ASTM B350-11.

3.1 The Cr-Zr binary system

The binary system of Cr-Zr is shown in Figure 2 [14]. Elemental chromium and zirconium have very high melting points of 1907 and 1855°C, respectively, but the phase diagram shows two eutectics with eutectic temperatures of 1559°C on the Cr-rich side and 1316°C on the Zr-rich side, which limit the maximum temperature at which a Cr-coating on a Zr-based cladding could endure. Even though pure chromium is grown on the Zr-based cladding, formation of the intermetallic Laves phase Cr_2Zr on the interface and diffusion of both elements require careful assessment of temperature limits for a modeling approach. The formation of a brittle laves phase was reported in recent publications [12,15,16]. The Laves phase for Cr coated Zircaloy cladding was found to consist mainly of $Cr_{2-x}Fe_xZr$ for HiPIMS coated material [16]. For

that reason, it is important to investigate the interface between the coating and cladding material and to determine the thickness of a formed intermetallic phase.
The formation of Cr_2Zr intermetallic may change the structural properties of Zr cladding. These changes could be aggravated by irradiation, temperature cycling, and/or accident scenarios and are typically not modeled, but they may be crucial to be incorporated if the Cr2Zr phase is showing a significant impact on the properties during normal operation and in case of accident scenarios. Therefore, integral LOCA tests on high-burnup fuel segments are required after a base study was conducted [17,18]. This report presents part of this base study.

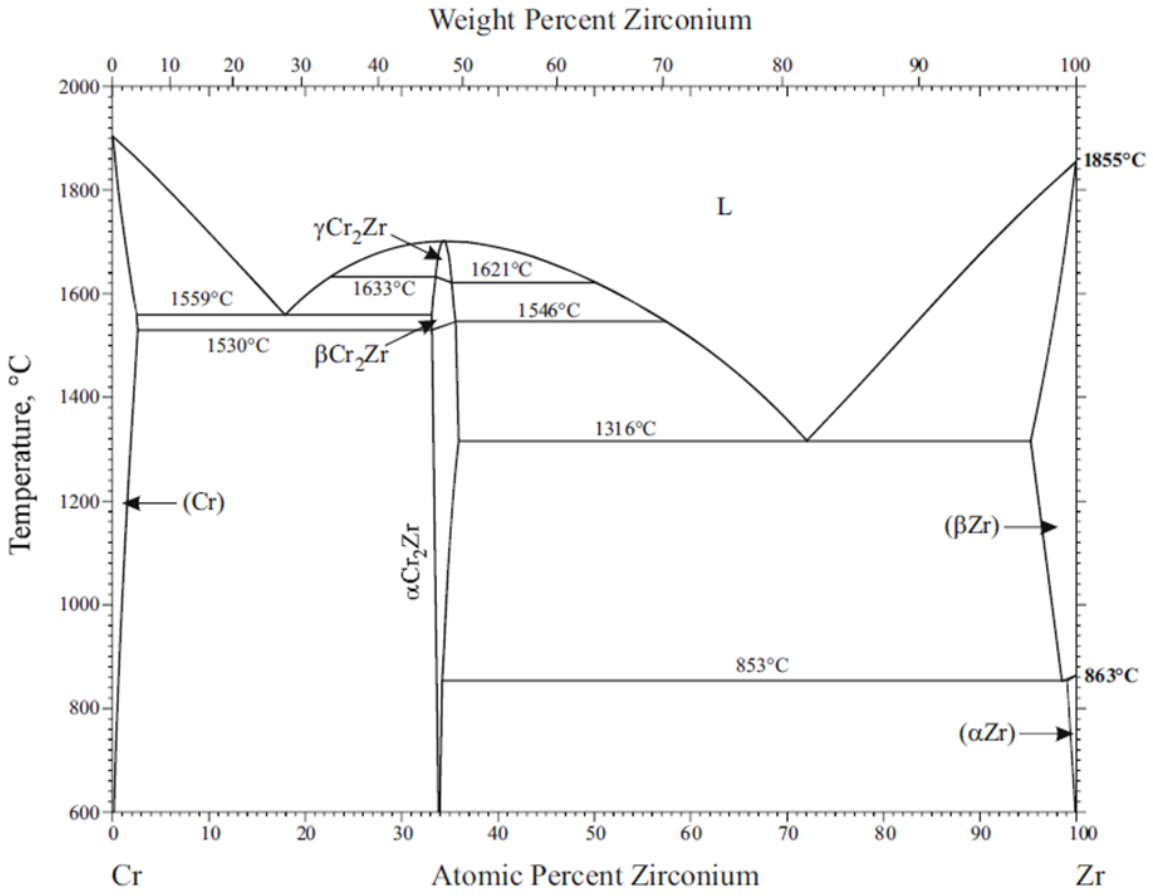

Figure 2. The binary Cr-Zr system [14,19].

3.2 SEM and TEM Analysis

Figure 3 shows the coated surface at different magnifications. HiPIMS PVD coating growth occurs very directional and mirrors the substrate surface [20]. The imperfections seen in the top left image of Figure 3 were introduced during the tube manufacturing process. The bottom left image shows some openings/ crack-like features. The surface structure displayed on the bottom right image is typical for a low temperature HiPIMS process. More insights about the microstructure and the coating density can be gained from SEM images from the cross-section of a coated tube as shown in Figure 4.
Here a location was selected which exhibits one of the aforementioned imperfections. Even though the coating is not showing any signs of ablation at low magnifications, the inset with a higher magnification reveals that the surface roughness of the substrate causes the formation of a crack. The directional growth, typical for HiPIMS coatings, combined with disability for the columnar grains to grow back together

across the trench leads to crack opening wherever the substrate material has imperfections i.e., scratches. Using HiPIMS at relatively low coating temperatures reduces the travel distance of atoms on the surface of the substrate, which inhibits an overgrowing of defects.

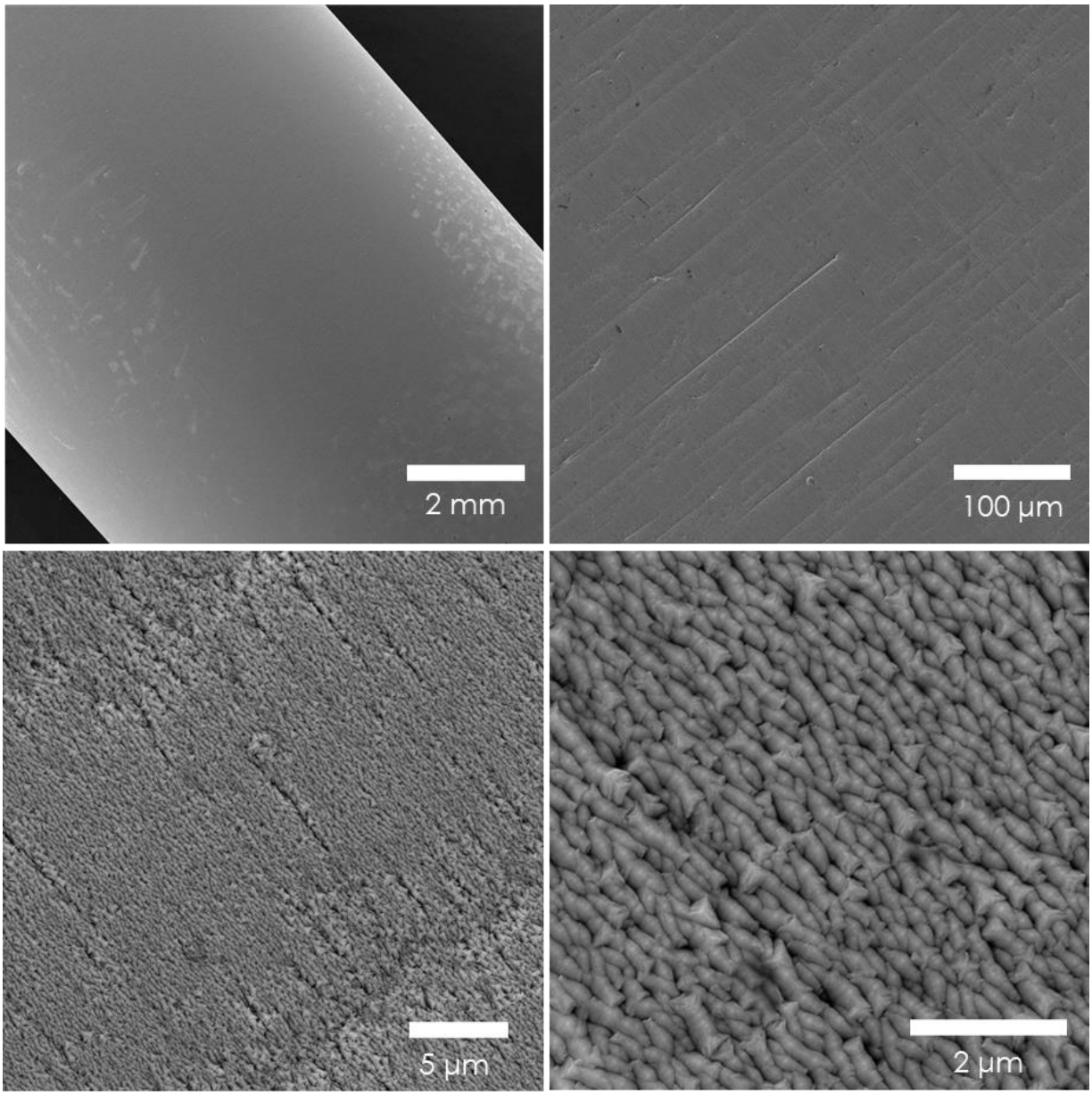

Figure 3 SEM image of the surface of a coated Zry-2 tube in 4 different magnifications. The coating is mirroring the surface finishing of the uncoated tube surface.

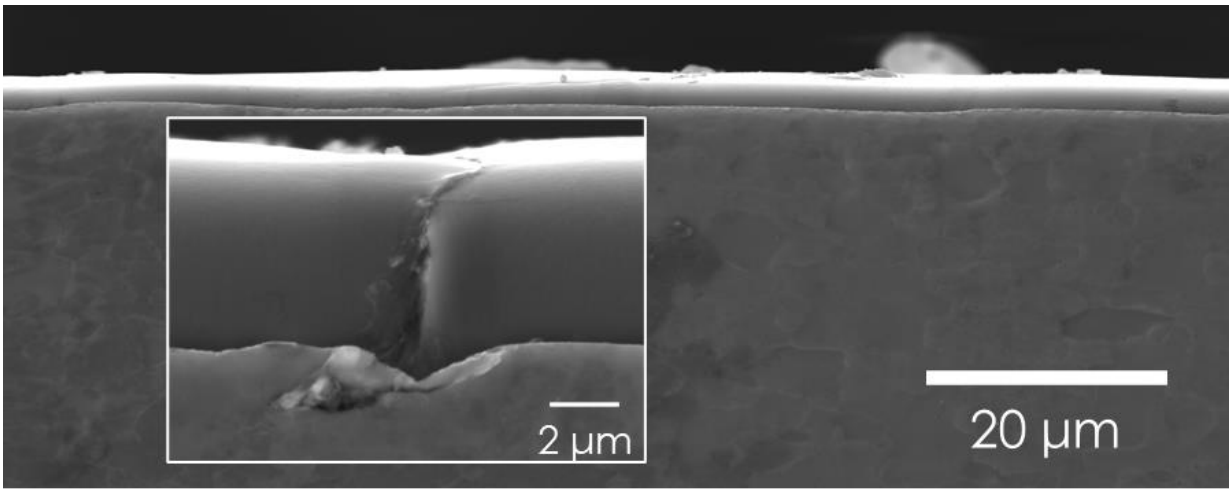

Figure 4 SEM image of a cross section of a 7-micron coating. The insert shows a crack in the coating caused by the surface roughness and the directional growth process of the coating during a HiPIMS process.

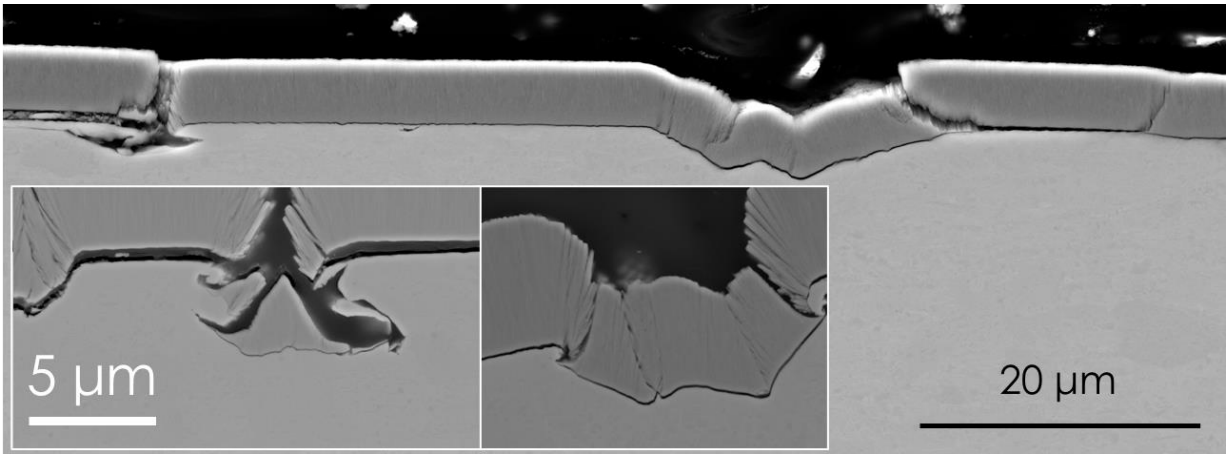

Figure 5 Cracked Cr coating on Zircaloy-4 found caused by the very rough surface.

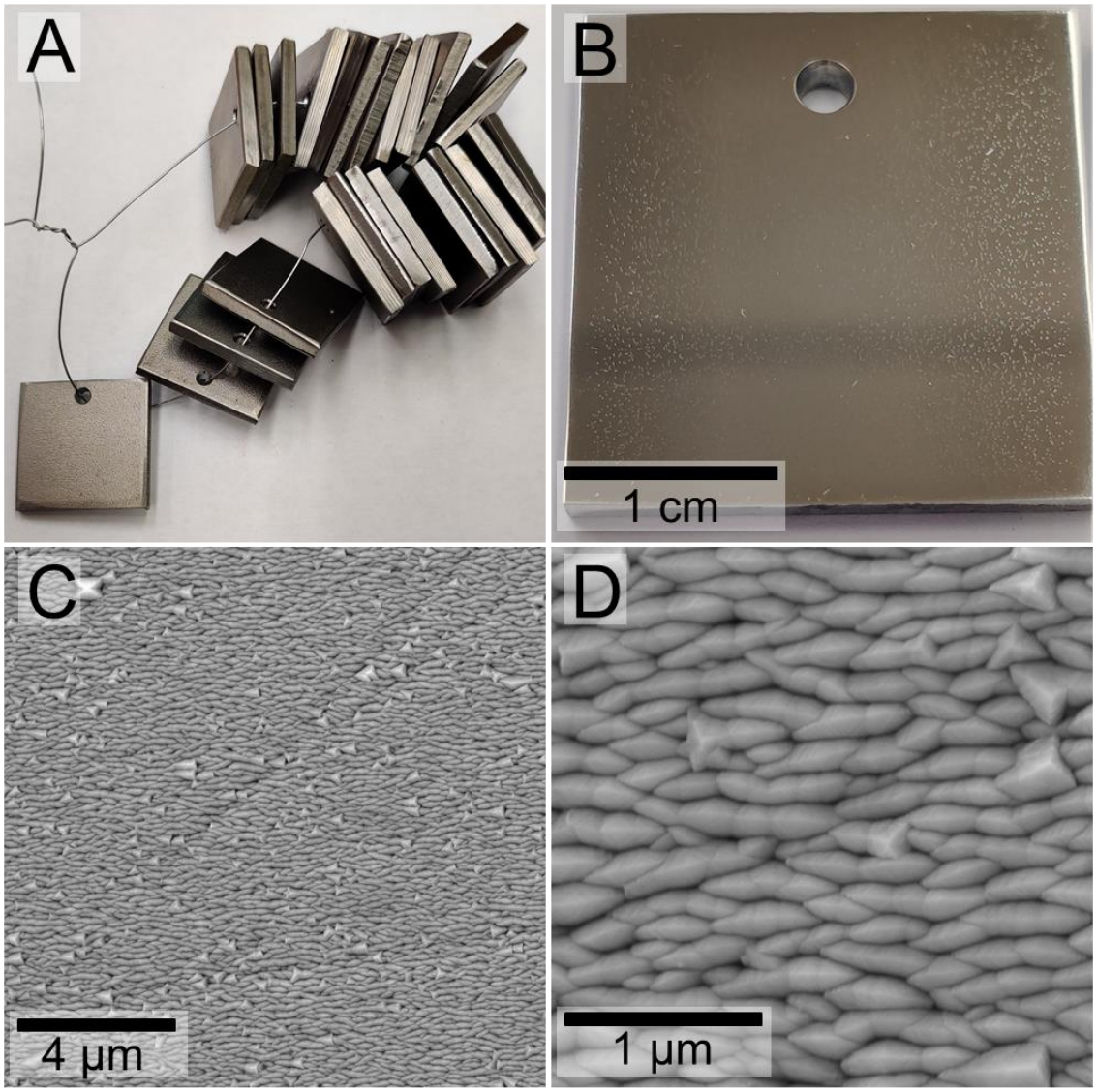

Figure 6 (A) uncoated Zry-4 coupons (B) polished coupon to a surface finish of 1 micron (C) Coated surface of a 1-micron finish is showing no cracking (D) Close-up of the Cr coating surface.

Cr-coating on the Zry-4 cladding material did not bond well enough, as shown in Figure 5. Two reasons for that were discovered: The high surface roughness, with scratches and grooves, caused by the tube pillgering process, exhibited in the inset in Figure 5. To investigate the roughness impact by a collaboration with Los Alamos National Laboratory, in addition to Cr-coated Zry-4 tubes, coupons of Zry-4 have been polished to roughnesses of 6, 3, 1, and 0.5 micrometer and coated using the same HiPIMS process parameters. A surface roughness of 1 micron or below was sufficient to create a crack-free coating as shown in Figure 6 (C). The surface roughness of 3 and 6 micron was not able to deliver a crack-free coating. However, because of the cracked coating on the Zry-4 tubes the emphasis for further investigations in this report was placed on coated Zry-2 tubes.
SEM EBSD was conducted on the coated Zry-2 cladding tubes to obtain grain size and orientation distribution information. Due to the fast oxidation of Zr and Cr, the tubes were polished to a colloidal silica finish using standard metallography techniques. The specimens were then cleaned and electropolished for 4 s in a solution of 60% methanol, 34% 2-butoxyenthonal, and 6% perchloric acid using a voltage of 20 V.

Immediately after the polishing process, the samples were analyzed using a TESCAN SEM and EDAX TEAM software. However, due to the different response to the etchant and the nano-sized grains in the Cr coating we were only able to record Kikuchi patterns for the Zry-2 base material. The inverse pole figure (IPF) map is shown on the right side of Figure 7. The left side of Figure 7 shows a secondary electron image of part of the EBSD mapped area. All values with a confidence index lower 0.1 were removed and a CI standardization cleanup was performed. An average area grain size of 4.8±2.0 μm and an average number grain size of 2.0±1.8 μm was calculated for Zry-2 using OIM Analysis software. The number average is the sum of (equivalent) diameters of each grain together and then divide by the total number of grains. The area average is calculated by multiplying the diameter of each grain by the area of the grain. Then the sum of this product for all of the grains is calculated and then divide by the total sum of the areas of all the grains.
The etching process was more prominent in the vicinity to the coating, which caused a rounding of the adjacent Zry-2 alloy clearly visible as a shading in that region. Because of that, the confidence index of the mapping in that area was below 0.1 which resulted non identified white area close to the coating in Figure 7.

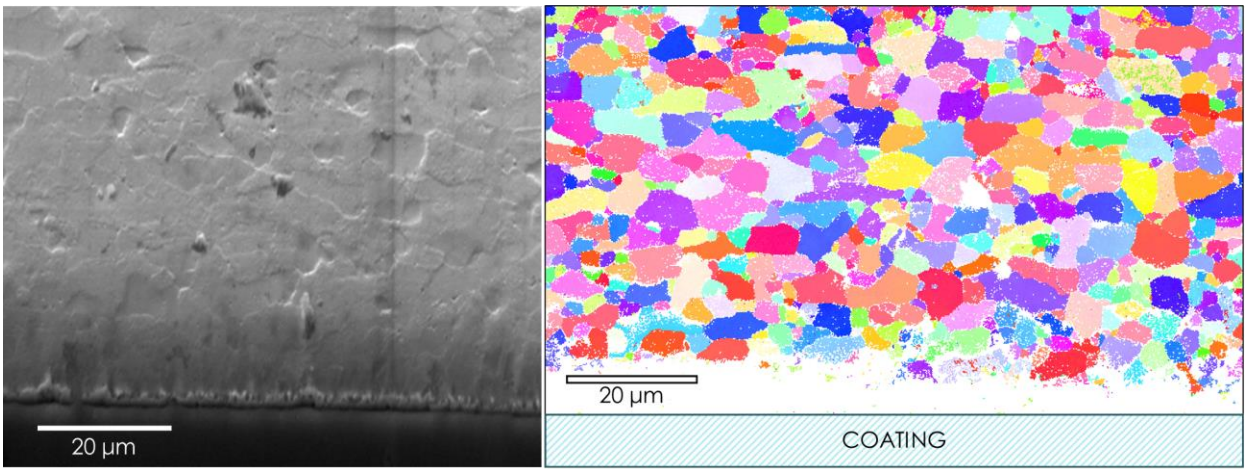

Figure 7 EBSD image of the Zircaloy-2 cladding close to the coating.

Specimens for transmission electron microscopy (TEM) were prepared using standard focused ion beam (FIB) preparation. Pt was deposited (3 micron thick, 2 micron in width, 20 micron in length) and the bulk lift-out of the sample was performed with using 20kV and 16nA for the trench cuts followed by a subsequent reduction of the current and voltage for the lift-out and thinning process. The final lamella was plasma cleaned before the sample holder was inserted in the TEM. Primary TEM was performed using an FEI (now Thermo Fisher Scientific) Talos F200X scanning transmission electron microscope (S/TEM) operating at 200 kV in ORNL's Low Activation Materials Development and Analysis (LAMDA) laboratory. Energy dispersive X-ray spectroscopy (EDS) was used to map interface region. Mapping was completed using a probe current of ~1 nA and a probe size of less than 1 nm with active drift correction every 10 s. The spectrum images were recorded using a 1024x1024 pixel region with a 3x3 neighborhood averaging filter applied during image post processing. Spectrum images were cropped in post-processing to generate the included figures.
A bright field (BF) TEM image with a magnification of 17500x is displaying the Zr and Cr interface on the left side of Figure 8. The top part of the left image of Figure 8 shows the lamellar structure of the Cr coating. A white box is highlighting the interface area, including area 1, which is magnified on the right-hand side. The bottom part is showing the Zr cladding material. The magnified area 1 presented on the right side was chosen because of its very thin region close to the interface, which are required for high resolution TEM imaging.

Small cracks seen between the columnar shaped Cr grains in the TEM image on the right-hand side of Figure 8 could let one assume that the coating regime was located in zone 1 in the generalized structure zone diagram shown in Figure 1. However, those thinner areas can also form during the TEM lamella preparation process using the ion bombardment of a FIB. Therefore, no unambiguous answer to the structure zone can be given just from the findings of thinner areas between the Cr grains.

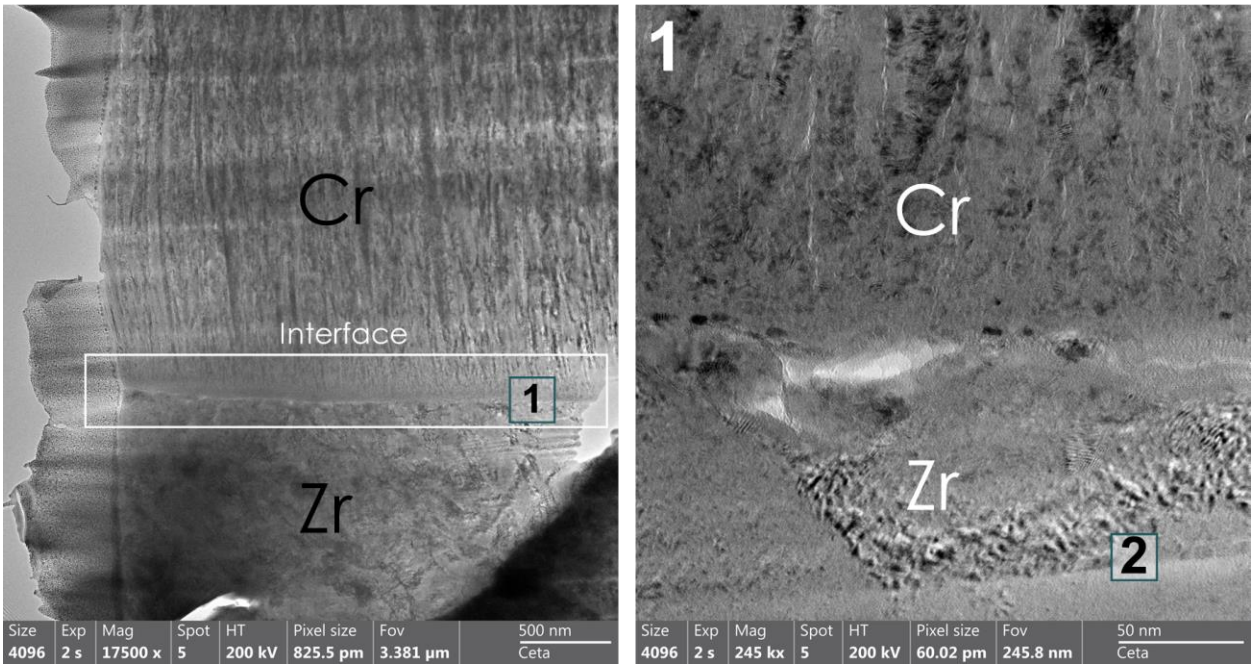

Figure 8. **Left:** BF TEM image of the Cr coating on top, Zr on the bottom, and the interface highlighted in the center. **Right:** Magnification of area 1 shown in the interface on the left image to investigate the interface.

Area 2 in Figure 8 was investigated to determine the grain orientation of the Zr cladding material close to the Cr interface and is shown in as a HRTEM image on the left side of Figure 9. The grain boundary between two grains is highlighted. The region FFT#1 was utilized to generate the Fast Fourier Transformation displayed on the right side of Figure 9. The SingleCrystal software package included in CrystalMaker Suite 2021 was used in combination with the ICSD database of alpha Zr (Collection Code 164572) to fit the diffraction pattern close to the [001] zone axis. The same process was utilized for the interphase region. The investigated area is shown on the left side of Figure 10, next to the FFT of the area labeled FFT#2. An FFT without any overlays is shown in the inset.
No laves phase was found in the very small, investigated region shown in Figure 10. To increase the region of interest, STEM EDS maps were taken across the interface to search for an increase in Fe, which reportedly is found together with Cr and Zr in the laves phase of HiPIMS coated Cr on Zircaloy. Information regarding the following phases were extracted from ICSD in addition to alpha-Zr mentioned before, to match the diffraction pattern shown in FFT#2: Cr (Collection Code 625717), Cr_2O_3 (Collection Code 258429), hexagonal laves phase Cr_2Zr, named C14, (Collection Code 106886), and cubic laves phase Cr_2Zr, named C15, (Collection Code 106885). The laves phase for Zircaloys usually contains Fe and contains precipitates of the type of $Zr(Fe,Cr)_2$ [21]. Those precipitates can be represented by the selected ICSD files.

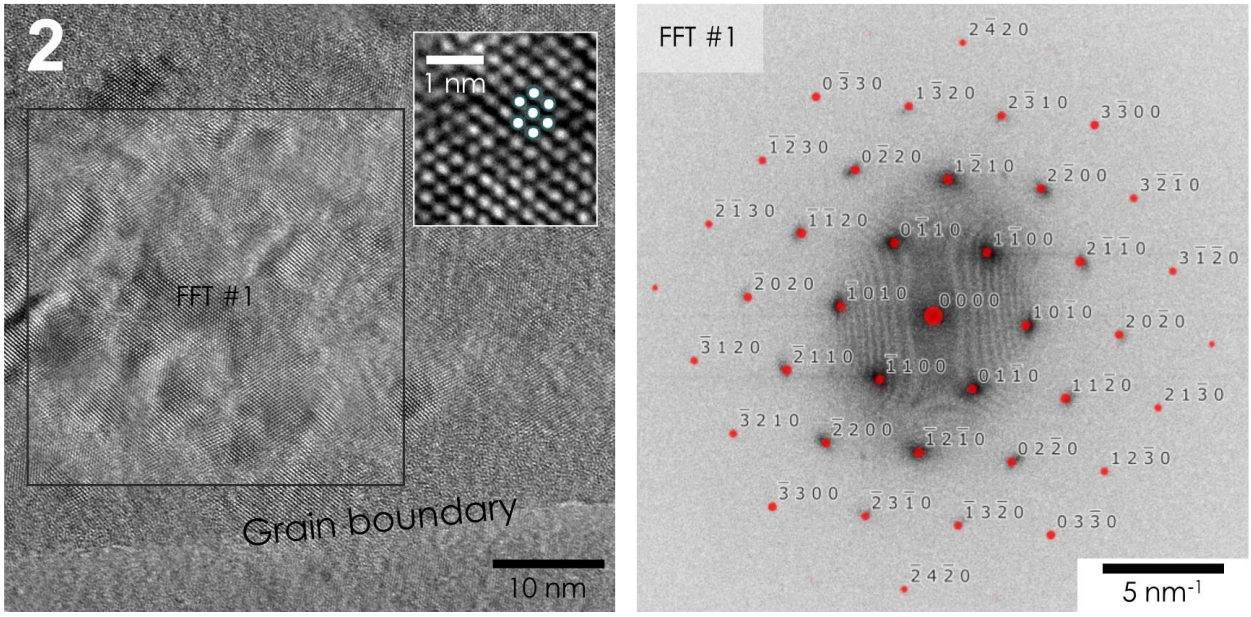

Figure 9. **Left:** Magnified area 2 of Figure 3 inside the Zr region adjacent to the interface. **Right:** FFT of the area shown on the left side to determine the orientation of the Zr grain. The hkl direction was determined to be close to the (001) zone axis.

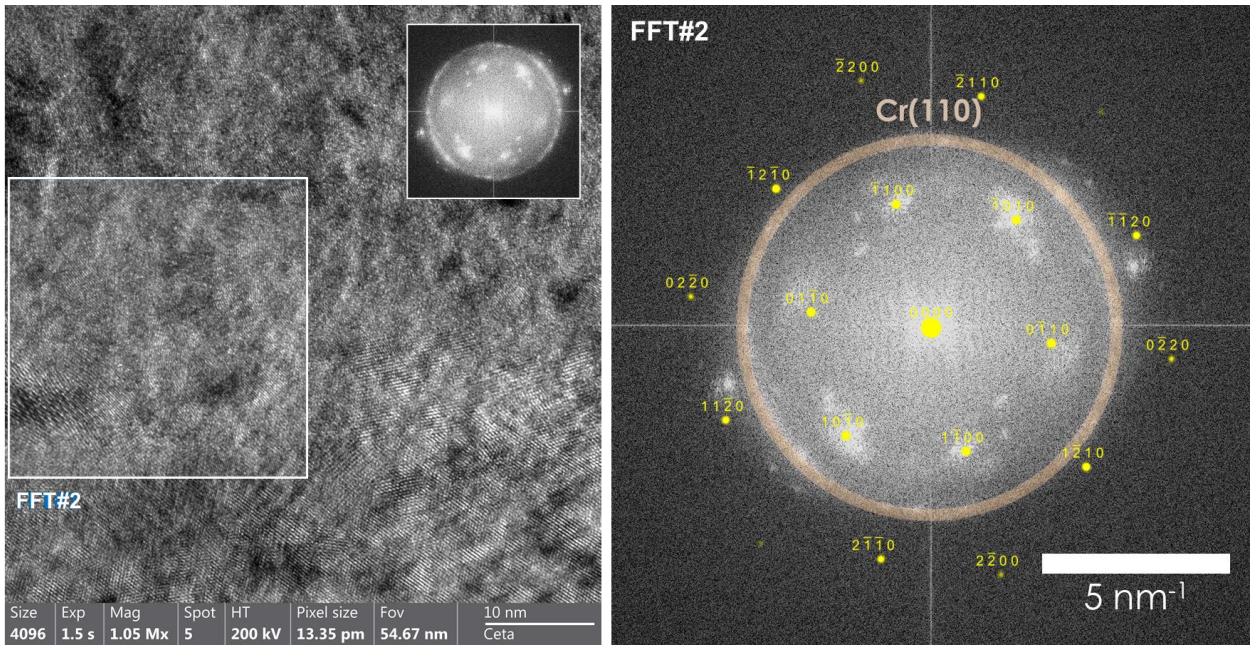

Figure 10. **Left:** HRTEM of the interface area. **Right:** FFT of the area#2 shown on the left side. The circle is a diffraction simulation of nanosized grains of the (110) plane of Cr. Several nano-sized Cr grains in that investigated area with random orientations were found. The alpha-Zr diffraction pattern was recorded close to the [001] zone axis.

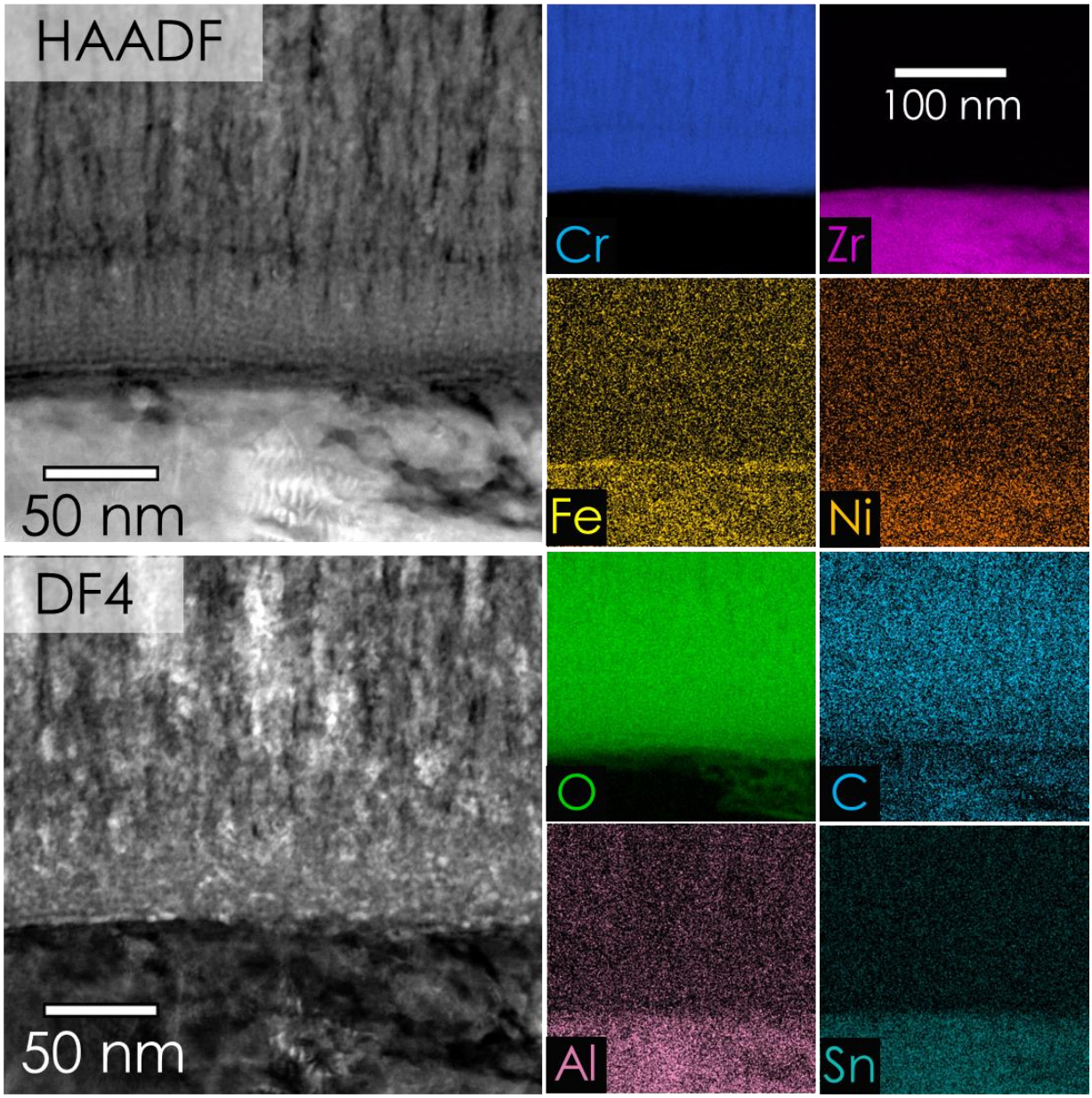

Figure 11 STEM HAADF and DF4 images next to elemental maps of the same area.

After calculating the lattice parameters for the mentioned phases for various Miller indices, the sole solution for the lattice distance of around 0.204 nm which is forming the circle highlighted in FFT#2 is the (110) lattice parameter of chromium. The formation of a circular diffraction pattern (typical for powder diffraction) with some brighter diffraction spots within the circle, means that randomly oriented nanosized grains of Cr have formed and can be found in the region of interest. Here, the only visible diffraction plane of Cr is a (110)-type. The previously fit of the alpha-Zr phase close to the [001] zone axis was added in yellow. Several other diffraction spots are visible and have been fitted against Cr_2Zr and Cr_2O_3. Chromia fits a couple of those spots but no intermetallic phase was found in the investigated region. Even though the laves phase can exist at room temperature according to phase diagrams, the formation of this phase requires energy i.e., in form of elevated temperatures. For that reason, it can be assumed that the coating process temperatures of 150 °C were not high enough to form the intermetallic

layer. Figure 11 is showing the results of the EDS scan as element maps on the right side, next to the HAADF and the DF4 images of the same region. Ni, Sn, and Fe are minor elements in Zry-2 alloy, according to Table 1, while C and Al are considered impurities. The amount of Fe seems to be increased at the interface, which made a more detailed investigation necessary.
Two line scans across the interface have been conducted. The major elements of Cr and Zr, together with oxygen, are shown for one of the line scans in Figure 12. These elements follow the same trend for other line scans (not displayed). A strong incline of each element is shown within a range of around 20 nm, respectively. This behavior is typical for the interface and was reported elsewhere [15]. Counts of the energy related to the Fe-K_{alpha} shells are shown in Figure 13 for both line scans. Here a small peak can be identified at the interface with a width of around 16 to 20 nm. This increase correlates with the increase of Fe exhibited at the interface in Figure 11. Even though a laves phase was not identified using HRTEM, it can be assumed that a very narrow region of less than 20 nm of the laves phase has formed. A complete absence of the intermetallic phase would mean that only a weak chemical bonding between the coating and cladding occurred, which seems unlikely due to the results shown in the nanoindentation section. In any case, the complete absence of an intermetallic phase after the coating process would not infer that the intermetallic will not form during normal operating temperatures, which is subject of further investigations.

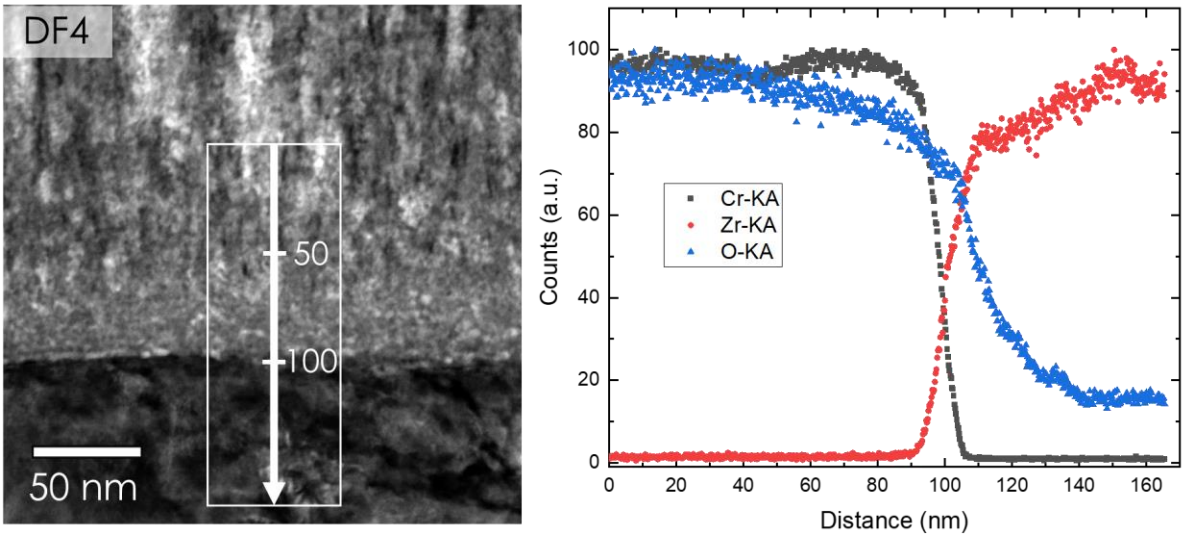

Figure 12. STEM Dark field 4 image with a 165 nm EDS line scan across the interface showing the major elements.

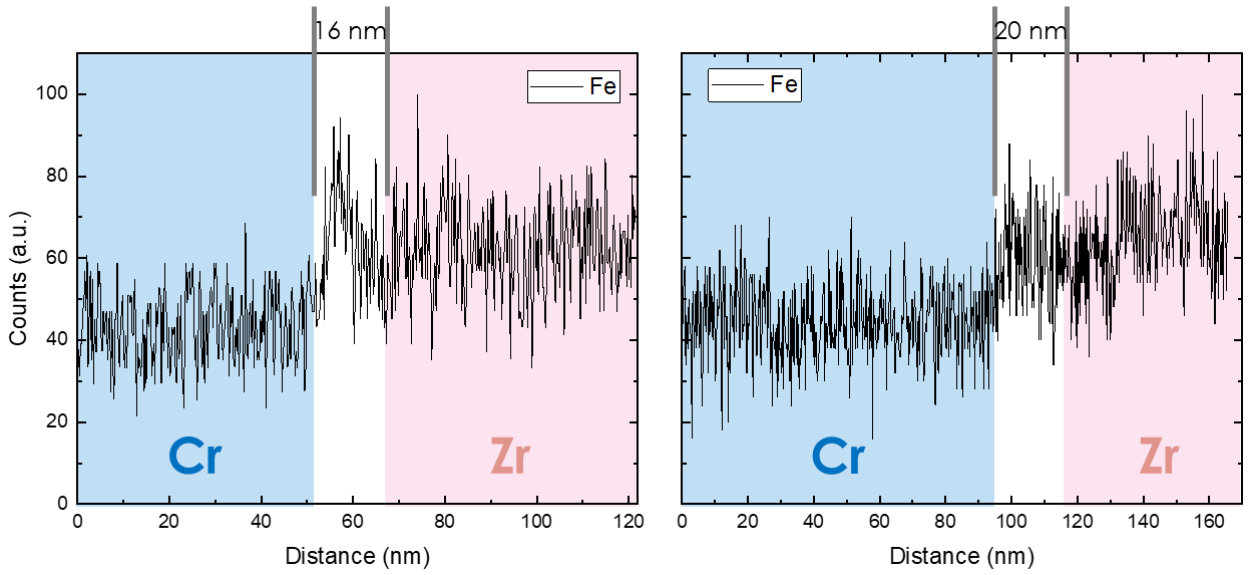

Figure 13 Line scans plotted for Fe across the interface. A small peak is shown right at the interphase between Cr and Zry-2.

3.3 Nanoindentation

Nanoindentation methods were used to determine the hardness and the elastic moduli of coating and cladding material. It is a rather inexpensive testing method, which can quickly be deployed to examine the interface evolution (laves phase) of irradiated materials. For comparison reasons with the irradiated samples, the coated cladding material was investigated in as-produced state.
A small tip in the shape of a 4-sided pyramid, called a Berkovich indenter, was pressed into the surface and load-displacement curves were recorded for each indentation. The measurements were performed on cross sections of coated tubes, polished to a mirror finish. During the polishing process the dislocation density in the polished surface region increases, which can lead to inflated hardness values. The Berkovich tip and the cross-section surfaces were cleaned before they were installed in the TESCAN SEM device. Single indentations and Nanoblitz map indentations were performed in coating and cladding material. The measurements were conducted load controlled following ASTM E2546 and conducted closed-loop load controlled [22]. A Poisson ratio of 0.37 was assumed for all measurements on Zry-2, while a passion ratio of Cr of 0.22 was utilized [23].
Literature values of the mechanical properties of Cr, Zry-2, and Zry-4 are listed in Table 2. It is important to mention that hardness values of Cr-coatings were reported to be highly depended on the grain size and the coating process parameters [24–26]. Figure 14 shows the single indentations in the coating, next to the Nanoblitz map nanoindentations, under a 71° viewing angle. The imaging conditions are constrained due to the necessary space of the nanoindenter inside the SEM, which only allows for a maximum tilt of 19°.

Table 2. Literature values of the mechanical properties of coating and cladding material.

Values	**Cr Coating**[23–26]	**Zry-2**[27,28]	**Zry-4**[29,30]
Hardness [GPa]	**2.85-14.2**	**1.8-2.2** (extrema: 1.59-2.99)	**2.0 – 3.0**
E-Modulus [GPa]	**140 – 300**	**95-110**	**99-115**

For that reason, the viewing angle is limited to 71° during nanoindentation. The Nanoblitz mapping is performed in a rectangular area, shown as a parallelogram due to the viewing angle, on the right side of Figure 14. A part of the indentation area was off the tube and coating (highlighted in pink) due to the curvature of the tube, which was taken into account for the evaluation of those maps. Figure 15 shows the hardness and elastic modulus plotted against the maximum indentation depth for 11 single indentations in the coating material. The hardness and E-Modulus are dependent on the depth of the indent and a deep enough indentation is required to minimize surface effects. A reasonable indentation depth for the coating was difficult to define: a small indentation depth results in a strong surface effect, while a large depth stretches the tested area into the cladding and surface of the tube. An impacted area of an indent is around 5 times the indentation depth as a radius, which would limit the depth to a maximum of 700 nm assuming the indentation is perfectly placed in the center of the coating [31]. The coating thickness varies and was found to be only 5 micron in some cases, which would further reduce the indentation depth to 500 nm. According to Figure 15, a depth of 500 nm is able to deliver reasonable results, with a slightly increased spread of the results. The results of single indentations of the coating are presented in Figure 15 and Figure 16 for the coating and in Figure 17 for the cladding material. Those values can be used for future qualification and simulation efforts, including BISON. The left image of Figure 15, i.e. shows a box plot and a normal curve distribution of the measured single indentation hardness results. 50 percent of the tests resulted in a hardness between 10.7 and 13.5 GPa. Similar values of the mean and median are found for all tests, which infer that the application of normal curve distribution is reasonable

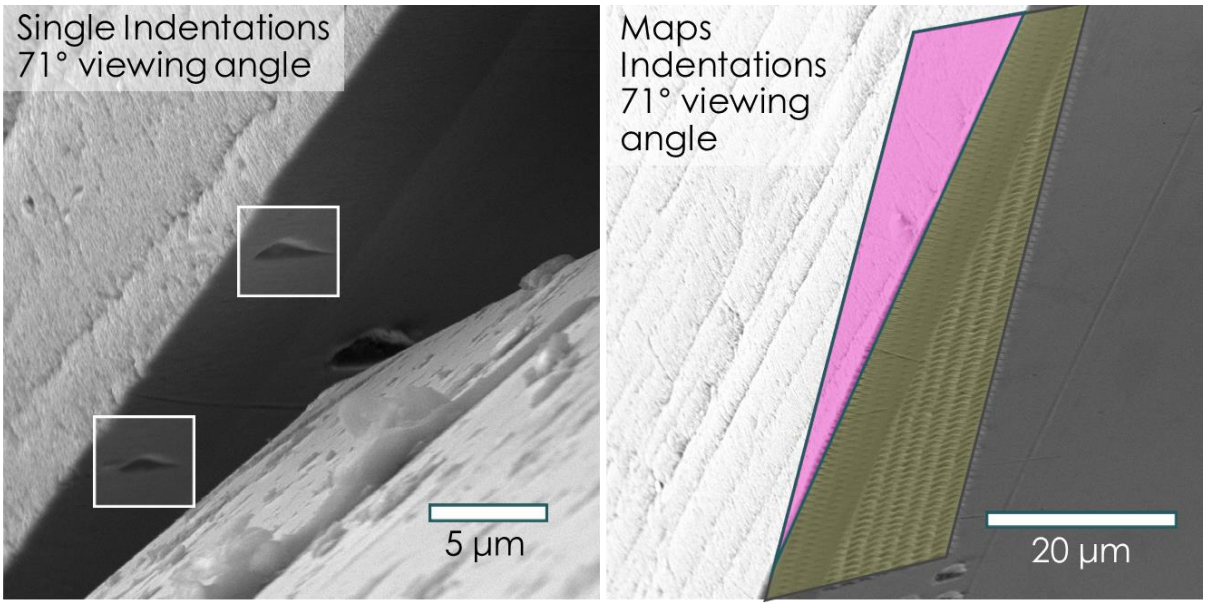

Figure 14 **Left:** Single indent highlighted inside the coating. **Right:** Nanoblitz mapping highlighted by the parallelogram area. Due to the curvature of the tube and the spacial limitations for nanoindentation inside a SEM a part of the nanoindentation maps were off the sample (pink), which needed to be considered when evaluating those maps.

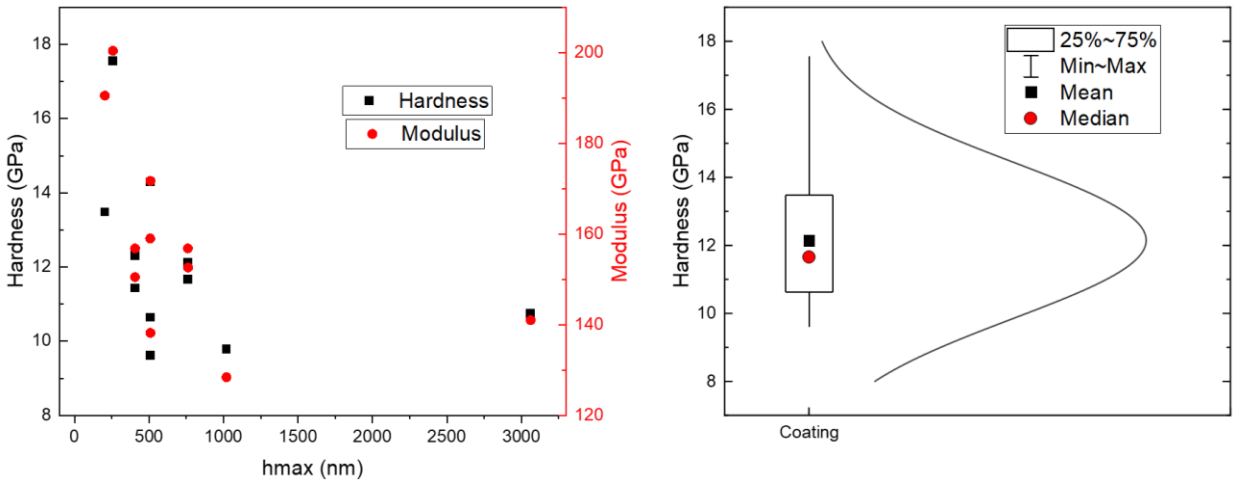

Figure 15. **Left:** Hardness and E-Moduli of the Cr-coating plotted against the maximum indentation depth. **Right:** Statistical evaluation of the single indentations in the coating show a mean and median value for the hardness close to 12 GPa.

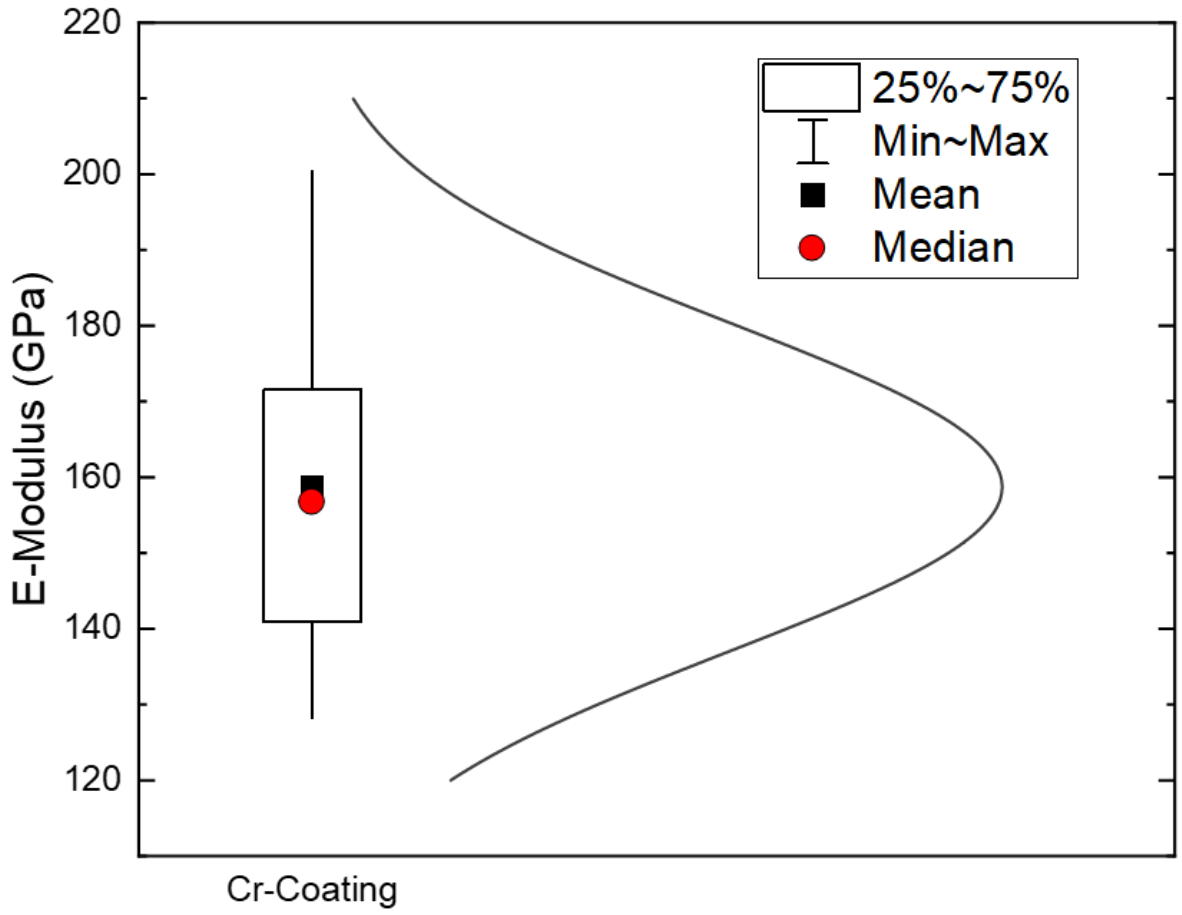

Figure 16 E-Modulus of the Cr-Coating taken from 11 single indentations.

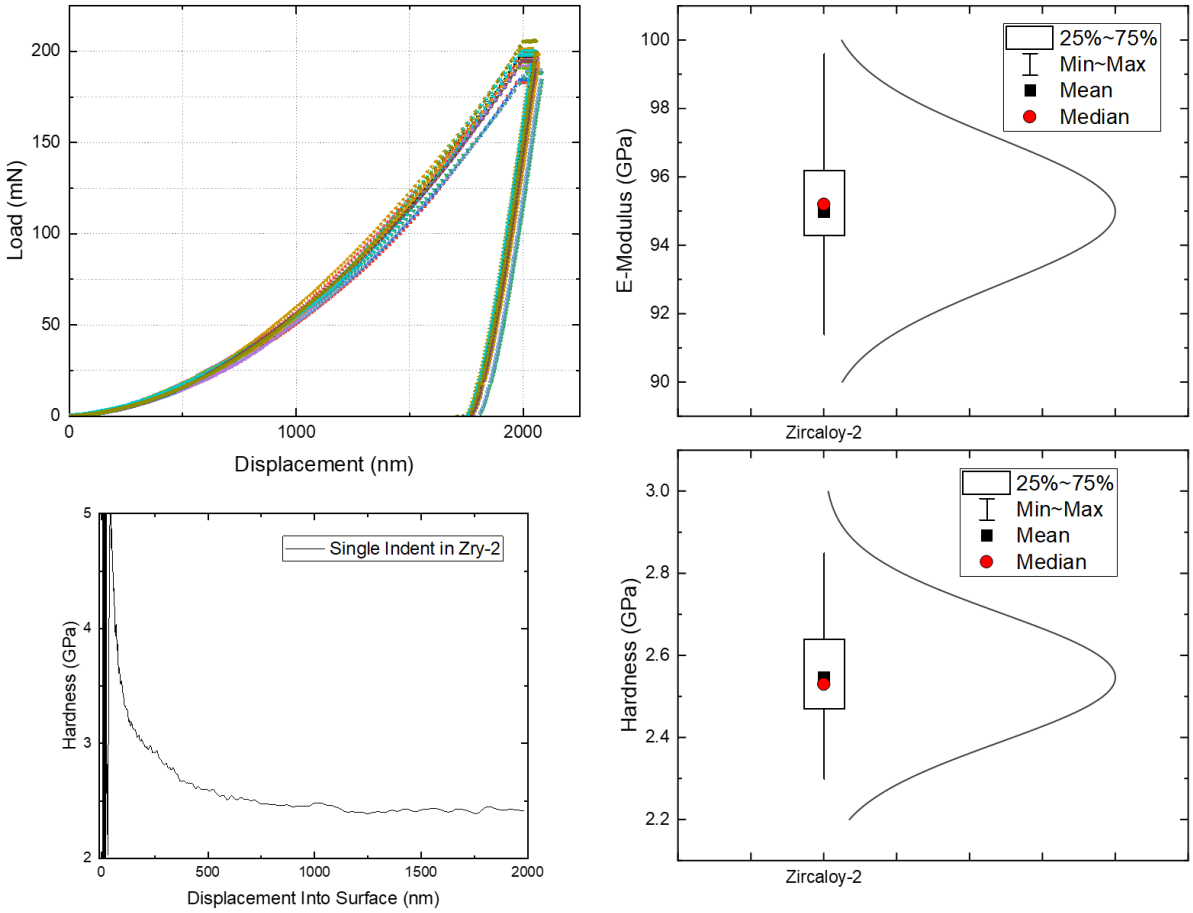

Figure 17. Hardness and E-Modulus determination of Zry-2 from 21 single indentation load-displacement curves. The hardness-displacement curve in the bottom left shows that an indentation depth of 400 to 1200 nm is valid for the calculation of the hardness. The images on the right side show a box plot and the normal curve distribution of the elastic modulus and the hardness of Zry-2.

Instrumented nanoindentations with a reduced load of 14 mN were used for mappings across the interface between coating and cladding to investigate the hardness distribution. A distance of 1000 nm between each point of indentation was selected, knowing that the indents may have an impact on each other. A distance of around 1500 to 1800 nm between each indentation for an indentation depth of 150 to 180 nm is recommended to prevent any interferences [31]. This decision was made to increase the number of indents, while reaching a high enough indentation depth to record valid values for hardness and elastic moduli. For that reason, values shown in Figure 15Figure 16Figure 17 should be used for simulation efforts. The results of the hardness and E-Moduli of instrumented mappings are shown in Figure 18 and Figure 19 and are used as comparative values within an area. Figure 18 displays the hardness of the coating in red in a range between 13 and 23 GPa, while Zry-2 in the blue region displays a uniform hardness of around 3 to 4 GPa. Due to a lower indentation depth and an increased impact of the surface, higher values across the board were measured for hardness and E-Moduli in coatings and claddings in comparison to the single indentations. The green area (x-position 0 to 10) in Figure 18 can be ignored, because no valid indentations were performed in that region. The tip of the indenter was located off the edge of the coated tube and the edge and not the tip of the Berkovich indenter was cutting into the coating which led to those meaningless values in the green area. The same region for Figure 19 can be ignored. The elastic modulus of the cladding with around 100 GPa, and a value of around 200 to 250 GPa for the Cr cladding are in agreement with the literature values.

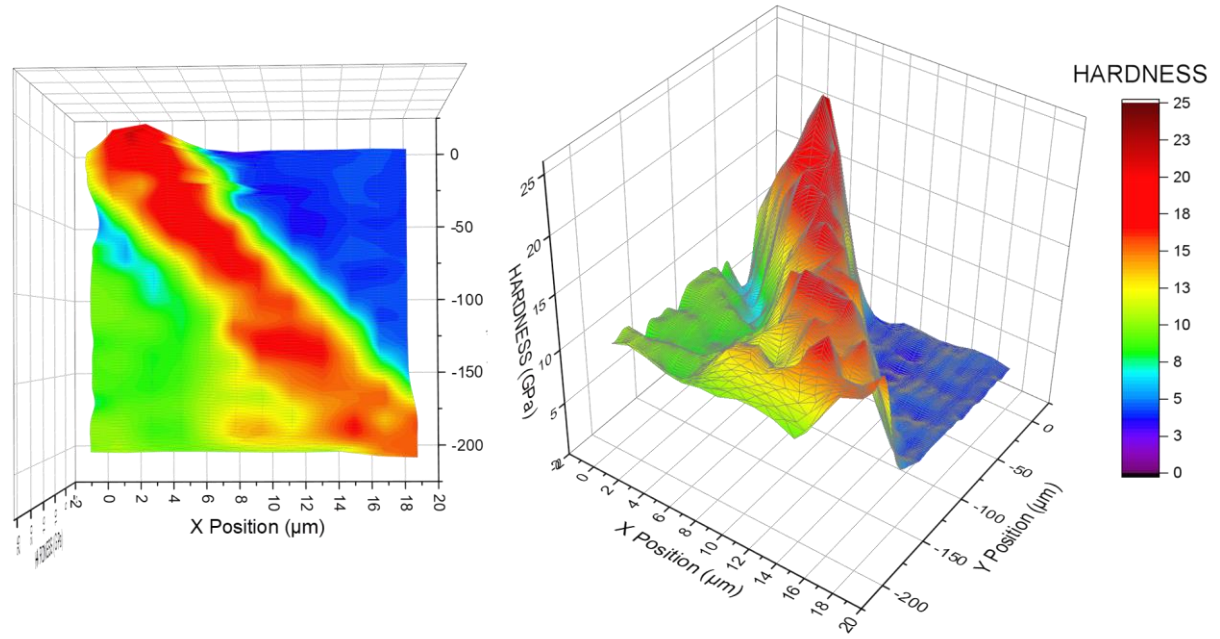

Figure 18. Nanoindentation mapping results showing the hardness in GPa of the Cr-coating and the Zry-2 cladding. The hardness of the Cr coating is in the range between 14 and 22 GPa. A smoothing factor of 0.2 was applied to the plotting.

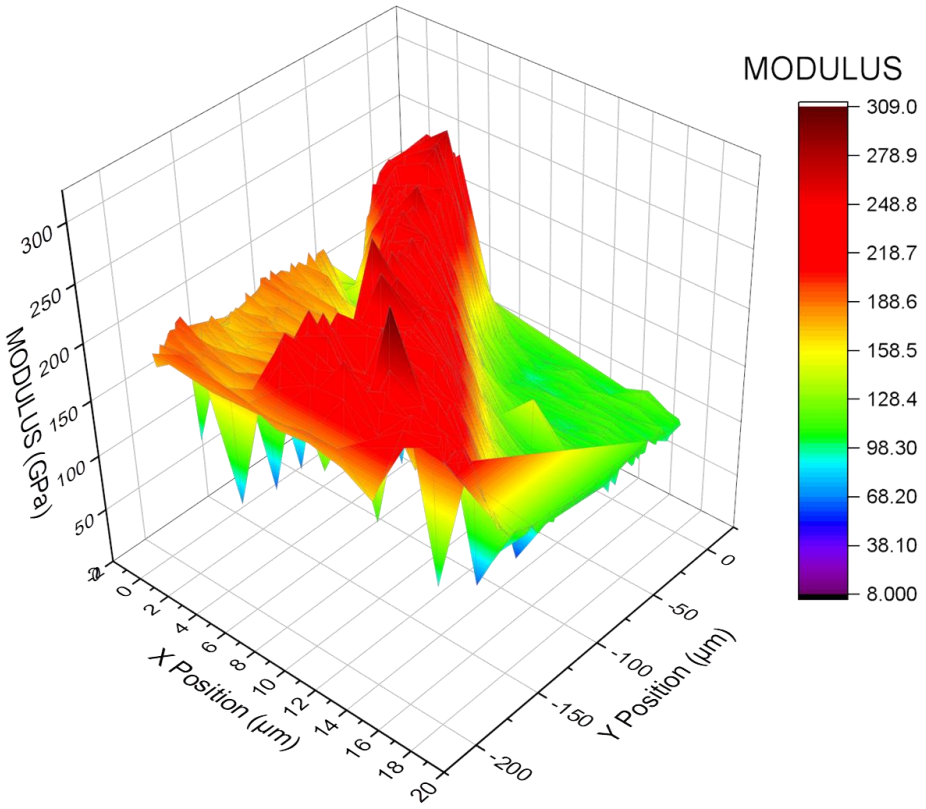

Figure 19. Nanoindentation results were used to calculate the E-moduli for each investigated position.

4. SUMMARY

Zry-4, Zry-4 coupons, and Zry-2 tubes and have been coated with a 5, 7, and 7 micrometer Cr coating using PVD HiPIMS methods, respectively. Investigations on the coupons with different roughnesses let us conclude that the higher surface roughness of the Zry-4 tubes led to severe crack formation of the directional grown coatings. However, defects were prominent in most methods applied to the received materials. For the generation of code qualification relevant data, the testing was focused on the HiPIMS Cr-coatings with a thickness of around 7 microns on Zircaloy-2 cladding, which exhibited only minor defect formation. Microstructure analysis were performed using SEM and TEM techniques, while nanoindentation methods were used to determine the hardness and elastic modulus of the coating and cladding material. SEM results demonstrate that the directional growth of the Cr coating combined with a rough surface area of the cladding material and low coating growth temperatures leads to cracks in the coating. TEM results revealed an increase of Fe on the interface, which suggests that a thin layer of a laves phase with less than 20 nm in thickness has been formed. However, due to the very thin region and the nanosized grains, those findings could not be proven by HRTEM images. Nanoindentation results provided hardness and elastic moduli values for coated cladding materials. The used methods were able to deliver reasonable data points, which can be used for simulation efforts in the qualification of coated ATFs. Future FY21 work will be performed on HiPIMS coated Zry-2 and Zry-4 tubes to investigate the burst behavior of partly cracked coatings, while further coating methods like cold sprayed Cr are applied to deliver code qualification work for coated cladding materials.

5. REFERENCES

[1] K.A. Terrani, Report on Design and Failure Limits of SiC/SiC and FeCrAl ATF Cladding Concepts under RIA Approved for public release, (2018).

[2] C. Tang, M. Stueber, H.J. Seifert, M. Steinbrueck, Protective coatings on zirconium-based alloys as accident-tolerant fuel (ATF) claddings, Corros. Rev. 35 (2017) 141–165. https://doi.org/10.1515/corrrev-2017-0010.

[3] M. Kurata, Research and Development Methodology for Practical Use of Accident Tolerant Fuel in Light Water Reactors, Nucl. Eng. Technol. 48 (2016) 26–32. https://doi.org/10.1016/j.net.2015.12.004.

[4] P. Hosemann, Small-scale mechanical testing on nuclear materials: bridging the experimental length-scale gap, Scr. Mater. 143 (2018) 161–168. https://doi.org/10.1016/j.scriptamat.2017.04.026.

[5] T. Shinozaki, Y. Udagawa, T. Mihara, T. Sugiyama, M. Amaya, Improved-EDC tests on the Zircaloy-4 cladding tube with an outer surface pre-crack, J. Nucl. Sci. Technol. 53 (2016) 1426–1434. https://doi.org/10.1080/00223131.2015.1123658.

[6] T. Jezequel, Q. Auzoux, D. Le Boulch, M. Bono, E. Andrieu, C. Blanc, V. Chabretou, N. Mozzani, M. Rautenberg, Stress corrosion crack initiation of Zircaloy-4 cladding tubes in an iodine vapor environment during creep, relaxation, and constant strain rate tests, J. Nucl. Mater. 499 (2018) 641–651. https://doi.org/10.1016/j.jnucmat.2017.07.014.

[7] H. Li, T. Koyanagi, X. Hu, Y. Katoh, Multiscale experimental characterization of coatings on ceramics: A case study of tungsten on SiC, Surf. Coatings Technol. 367 (2019) 1–10. https://doi.org/10.1016/j.surfcoat.2019.03.040.

[8] J. Chen, S.J. Bull, Approaches to investigate delamination and interfacial toughness in coated systems: An overview, J. Phys. D. Appl. Phys. 44 (2011). https://doi.org/10.1088/0022-3727/44/3/034001.

[9] H. Chen, X. Wang, R. Zhang, Application and development progress of Cr-based surface coating in nuclear fuel elements: II. Current status and shortcomings of performance studies, Coatings. 10 (2020). https://doi.org/10.3390/coatings10090835.

[10] A.-M. Velente-Feliciano, Hipims : A New Generation of Film Deposition Techniques for Srf Applications, Proc. SRF2013. (2013) 754–760.

[11] J.C. Brachet, I. Idarraga-Trujillo, M. Le Flem, M. Le Saux, V. Vandenberghe, S. Urvoy, E. Rouesne, T. Guilbert, C. Toffolon-Masclet, M. Tupin, C. Phalippou, F. Lomello, F. Schuster, A. Billard, G. Velisa, C. Ducros, F. Sanchette, Early studies on Cr-Coated Zircaloy-4 as enhanced accident tolerant nuclear fuel claddings for light water reactors, J. Nucl. Mater. 517 (2019) 268–285. https://doi.org/10.1016/j.jnucmat.2019.02.018.

[12] J. Ribis, A. Wu, J. Brachet, E. Clouet, B. Arnal, E. Rouesne, S. Urvoy, F. Barcelo, A. Gentils, C. Baumier, L. Rancoeur, Y. Robert, F. Leprêtre, J. Bischoff, E. Pouillier, Chromium hardening and Zr-Cr interface stability of irradiated chromium-coated Zircaloy-4 alloy, (2018). https://hal-cea.archives-ouvertes.fr/cea-02400192 (accessed December 31, 2020).

[13] M. Wagih, B. Spencer, J. Hales, K. Shirvan, Fuel performance of chromium-coated zirconium alloy and silicon carbide accident tolerant fuel claddings, Ann. Nucl. Energy. 120 (2018) 304–318. https://doi.org/10.1016/j.anucene.2018.06.001.

[14] H. Okamoto, Supplemental Literature Review of Binary Phase Diagrams: B-Fe, Cr-Zr, Fe-Np, Fe-W, Fe-Zn, Ge-Ni, La-Sn, La-Ti, La-Zr, Li-Sn, Mn-S, and Nb-Re, J. Phase Equilibria Diffus. 37

(2016) 621–634. https://doi.org/10.1007/s11669-016-0465-z.

[15] A. Wu, J. Ribis, J.C. Brachet, E. Clouet, F. Leprêtre, E. Bordas, B. Arnal, HRTEM and chemical study of an ion-irradiated chromium/zircaloy-4 interface, J. Nucl. Mater. 504 (2018) 289–299. https://doi.org/10.1016/j.jnucmat.2018.01.029.

[16] J. Ribis, A. Wu, J.C. Brachet, F. Barcelo, B. Arnal, Atomic-scale interface structure of a Cr-coated Zircaloy-4 material, J. Mater. Sci. 53 (2018) 9879–9895. https://doi.org/10.1007/s10853-018-2333-1.

[17] M.N. Cinbiz, B. Garrison, R.R. Lowden, R.G. Sitterson, K. Linton, Progress Report on Modified Burst Testing and Alternative Test Methodologies, (2019). https://www.osti.gov/servlets/purl/1530086.

[18] J. Brachet, M. Dumerval, M. Le Saux, E. Rouesne, S. Urvoy, T. Guilbert, Q. Houmaire, C. Cobac, Behavior of chromium coated M5TM claddings under loca conditions To cite this version : HAL Id : hal-02419638, WRFPM 2017 Water React. Fuel Perform. Meet. (2017).

[19] H.J. Lu, W.B. Wang, N. Zou, J.Y. Shen, X.G. Lu, Y.L. He, Thermodynamic modeling of Cr-Nb and Zr-Cr with extension to the ternary Zr-Nb-Cr system, Calphad Comput. Coupling Phase Diagrams Thermochem. 50 (2015) 134–143. https://doi.org/10.1016/j.calphad.2015.06.002.

[20] A.K. Evans, P.J. Kelly, D.T. Goddard, E.P. Vernon, Fabrication, characterisation and testing of cr coated zr alloy nuclear fuel rod cladding for enhanced accident tolerance, Light Water React. Fuel Perform. Conf. (TOP FUEL 2019). (2020) 864–872.

[21] F. Stein, A. Leineweber, Laves phases: a review of their functional and structural applications and an improved fundamental understanding of stability and properties, J. Mater. Sci. 56 (2021) 5321–5427. https://doi.org/10.1007/s10853-020-05509-2.

[22] J. Chen, L. Lu, K. Lu, Hardness and strain rate sensitivity of nanocrystalline Cu, Scr. Mater. 54 (2006) 1913–1918. https://doi.org/10.1016/j.scriptamat.2006.02.022.

[23] M. Ševeček, A. Gurgen, A. Seshadri, Y. Che, M. Wagih, B. Phillips, V. Champagne, K. Shirvan, Development of Cr cold spray–coated fuel cladding with enhanced accident tolerance, Nucl. Eng. Technol. 50 (2018) 229–236. https://doi.org/10.1016/j.net.2017.12.011.

[24] A. Brenner, P. Burkhead, C. Jennings, Physical properties of electrodeposited chromium, J. Res. Natl. Bur. Stand. (1934). 40 (1948) 31. https://doi.org/10.6028/jres.040.022.

[25] R. Fritz, D. Wimler, A. Leitner, V. Maier-kiener, D. Kiener, Acta Materialia Dominating deformation mechanisms in ultra fi ne-grained chromium across length scales and temperatures, 140 (2017) 176–187. https://doi.org/10.1016/j.actamat.2017.08.043.

[26] D.V. Sidelev, G.A. Bleykher, M. Bestetti, V.P. Krivobokov, A. Vicenzo, S. Franz, M.F. Brunella, A comparative study on the properties of chromium coatings deposited by magnetron sputtering with hot and cooled target, Vacuum. 143 (2017) 479–485. https://doi.org/10.1016/j.vacuum.2017.03.020.

[27] A. Lodh, P. Pant, G. Kumar, K. V. Mani Krishna, R. Tewari, I. Samajdar, Orientation-dependent solid solution strengthening in zirconium: a nanoindentation study, J. Mater. Sci. 55 (2020) 4493–4503. https://doi.org/10.1007/s10853-019-04280-3.

[28] K. Kese, P.A.T. Olsson, A.M. Alvarez Holston, E. Broitman, High temperature nanoindentation hardness and Young's modulus measurement in a neutron-irradiated fuel cladding material, J. Nucl. Mater. 487 (2017) 113–120. https://doi.org/10.1016/j.jnucmat.2017.02.014.

[29] S. Suman, M.K. Khan, M. Pathak, R.N. Singh, Investigation of elevated-temperature mechanical properties of δ-hydride precipitate in Zircaloy-4 fuel cladding tubes using nanoindentation, J.

Alloys Compd. 726 (2017) 107–113. https://doi.org/10.1016/j.jallcom.2017.07.321.

[30] C. Evans, Micromechanisms and Micromechanics of Zircaloy-4, London, 2014.

[31] P. Sudharshan Phani, W.C. Oliver, A critical assessment of the effect of indentation spacing on the measurement of hardness and modulus using instrumented indentation testing, Mater. Des. 164 (2019) 107563. https://doi.org/10.1016/j.matdes.2018.107563.